



Tian Gan · Qiong Wang · Wenjun Gan · Zhang Jieming

# Visualization study of perturbations induced by plasma actuators and its effect on shock wave/boundary-layer interaction

Received: 28 July 2022 / Revised: 8 October 2022 / Accepted: 11 October 2022 / Published online: 27 November 2022  
© The Author(s) 2022

**Abstract** Surface arc plasma actuator array is used to control the shock wave/boundary-layer interaction in a  $Ma = 2$  flow. Two types of interaction are examined. The flow topology of Surface arc plasma actuator array operating at high-frequency is firstly visualized via particle laser scattering (PLS) technique. The results show that two typical flow structures are observed in the discharging process: the thermal gas bubble and the trailing vortices. The high-frame low-exposure schlieren results for flow visualization indicate a significant separation inhibition in both experiments due to an improvement in the mixture upstream of the interaction region and promoting more turbulent structure into the boundary layer. In the baseline, the separation shock oscillates in a low-frequency mode. When plasma actuation is turned on, the spectra change dramatically when compared to the baseline condition without control. There is an apparent frequency shift for separation shock.

**Keywords** Separation control · Flow visualization · Plasma actuator · Surface arc

## 1 Introduction

Shock wave/boundary-layer interaction (SWBLI) is a fundamental flow that can be found in a variety of aerodynamic applications, including supersonic and hypersonic vehicles and high-speed turbo-machinery (Hadjadj and Dussauge 2009). SWBLI is usually undesirable because it has a number of negative consequences (Huang et al. 2020). A pressure loss is occurred as the boundary layer is separated because of strong adverse pressure gradient imposed by the shock. In the most extreme case, the supersonic inlet may experience a blockage due to massive of separation flow. The unsteadiness of SWBLI is also concerned by the researchers because it accelerates the consumption of service life of vehicles. The primary factor contributing to the unsteadiness is the flow that oscillates in a frequency band being defined as low-frequency unsteadiness (Clemens and Narayanaswamy 2014). Furthermore, additional pressure load will be imposed on the aero body of the vehicles which will create structure fatigue problems (Huang and Yao 2020).

Plasma-based actuators (PBAs) have been widely used in recent years due to their simplicity, adjustable frequency, and fast response (Wu and Li 2015). Furthermore, the controlling stratagems are more flexible using different types of actuators such as the surface arc discharge actuators (Gan et al. 2018a), sliding-arc filament plasma actuators (Liao et al. 2020), spark-jet actuators (Xie et al. 2021), dielectric barrier discharge actuators (Im et al. 2010), and radio frequency discharge plasma actuators (Kim et al. 2010). Narayanaswamy et al. (2012) demonstrated a frequency shifting in a ramp-induced SWBLI using

plasma discharge jet. The results show that the low-frequency unsteadiness has been partly removed according to the power spectra of wall-pressure measurements. Knowing its effectiveness in ramp SWBLI control, Webb et al. (2013) further studied SWBLI control using the plasma actuator with arc filaments. The control mechanism was examined in that paper, and it was concluded that the heat injection is a key impactor produced a boundary layer alteration. Yan and Gaitonde (2010) presented a numerical study of a shock interacting with a laminar boundary layer by using the same actuators. The actuators were designed as a rectangular surface heat source. Their findings revealed counter-rotating vortices are produced downstream of the heating region. It is believed that the vortices play an important role in the separation suppression. After that, it is believed that vortex forcing effect is the predominate mechanism while the actuator is operating in a low consumption mode. Tang et al. (2018) also found that hairpin-like vortices were generated behind the main gas bubble. These vortices were assumed to be a primary reason for shock intensity weakening. Wang et al. (2018) investigated the control effect of a plasma jet array on flow instability of a blunt nose. It was shown that the vortex ring generated by the actuators contributes to the momentum transfer upstream the corner, and the control effect is sensitive to the position where jets interact with the shear layer.

Surface arc plasma actuators (SAPAs) have gained an increasing interest because their advantages of simple geometry, high reputation rates, and flexibility in switch operation frequency. Luo et al. (2022) employed SAPAs in the control of incident shock wave that interacts with a laminar boundary layer. The results show that low-frequency unsteadiness inhibition deeply depends on the actuation frequency, while the low frequency has a higher performance than the high frequency in incident SWBLI. Tang et al. (2022a) recently observed that  $\Lambda$  vortices generated by SAPAs in tripped boundary layer behaved similarly to hairpin vortices generated by vortex generators (VGs) in a boundary layer that transitioned to turbulent state. Ma et al. (2022) numerically studied the mechanism of high-frequency SAPAs in a  $Ma = 2.5$  flow. The results indicated that the blast wave induced by SAPA also had an effect on the configuration of shock wave/boundary-layer interaction generated by a semi-cylinder, and the control capability depends on its input exciting power. In addition, a drag-reduction effect is also demonstrated by increasing exciting power or actuation frequency which make SAPA has a better application in prospect. Yang et al. (2022) carried out a numerical study to explore the effects of SAPA on three-dimensional shock wave/boundary-layer interaction by using a swept ramp in a Mach 2.95 flow. The effect of three actuator location on swept shock wave/boundary-layer interaction is examined. Each location showed well manipulation in flow topology but depends on different controlling mechanism. And recently, the SAPAs have attracted an extensive attention in hypersonic flow regime (Wang et al. 2022; Tang et al. 2022b). The separated flow and shock–shock interaction have been improved as SAPA is activated. The ability of SAPA on hypersonic flow control has been proved practicable.

Although the above studies have shown the ability to reduce some of the adverse effects related to the low-frequency unsteadiness, however, the results of separation inhibition are not substantially achieved. It is critical to investigate the influence of SAPAs (Surface arc plasma actuators) on separation control for shock wave/boundary-layer interaction. In summary, we conducted two experimental researches to investigate the separation control of SWBLI using SAPAs. Two types of SWBLI were tested in the experiment, namely, an incident shock wave/boundary-layer interaction (ISWBLI) and a ramp-induced shock wave/boundary-layer interaction (RSWBLI). The experiment focuses on an arc discharge with a reputation rate over two types of SWBLI to determine the separation control effect. After describing the experimental setup, the schlieren results, Planar laser scattering (PLS) results, electrical characteristic, and statistical results for shock motion are presented and discussed.

## 2 Experimental setup

The experimental data presented in this work were collected in a suction type supersonic wind tunnel, as shown in Fig. 1. The tunnel is driven by the pressure difference between the outside atmosphere and a vacuum tank with a volume of  $120 \text{ mm}^3$ . This wind tunnel uses a long controlling section (in blue), followed by a replaceable converging–diverging nozzle (in red) that accelerates the flow to the designed Mach number, and a test chamber (in yellow) with a vacuum tank (in pink) at the end of the tunnel. The tunnel nozzle was polished to a mirror finish to eliminate the wall interference effect and three-dimensional effects and achieve a quiet flow freestream with few pressure fluctuations. The axisymmetric nozzle has a 300 mm outlet diameter and expands the flow to  $Ma = 2$  in a 1.8 m diameter cylindrical test chamber. Two windows

were assembled on both sides of the test chamber flow visualization and one on the top for laser passing through. As a result, optical measurement techniques and laser perturbations can gain access to the test section's core area. The wind tunnel is started by a circular membrane-breaking device with an electrical switch. The pump sets consist of three pump types, including water ring pumps (operating range from 0.06 bar to the local atmospheric pressure), sliding vane pumps (operating range from 0.03 to 0.08 bar), and root pumps (operating below 100 Pa).

The air inside the vacuum tank was pumped out to achieve a vacuum with a pressure of 5–10 Pa, allowing running times of 1.5 s. A stable supersonic flow with a Mach number of 2.0 was generated during the experiments, with a total pressure of 95.6 kPa and a temperature of 296 K. In the core test region, the static pressure  $P_s$  and static temperature  $T_s$  were 12.24 kPa and 164 K, respectively. The velocity of the supersonic free stream was 513 m/s, which results in a unit Reynolds number of  $1.13 \times 10^7 \text{ m}^{-1}$ . The operating parameters of this facility are presented in Table 1.

The characteristic of shock wave/boundary-layer interaction can be visualized by many experimental photography techniques including schlieren system (Zhang et al. 2021) or schlieren system with color (Maeno et al. 2000). In this study, a Z-type light route was used in the schlieren investigations, as shown in Fig. 2. A Gloria 500 W Xenon bulb provided illumination. The schlieren images were captured with a Phantom V2512 ultra-high-speed camera with a maximum resolution of  $1280 \times 800$  pixels. Because the knife-edge is vertically positioned, the schlieren is sensitive to horizontal density gradients. The maximum image acquisition frequency is 700,000 Hz with  $1 \mu\text{s}$  minimum exposure time to freeze the flow features.

Schlieren diagnostics is a qualitative flow visualization technique for flow structures with a density gradient. In a previous study (Gan et al. 2018b), we first proposed using the mean ( $I_{\text{mean}}$ ) and the root mean square (RMS) ( $I_{\text{rms}}$ ) of the schlieren intensity, resulting in flow structures with very shape edges in ramp supersonic flow. Briefly, the principle of this method is based on flow fluctuation, reflected by the variance of the intensity in the schlieren image. The intensity in a schlieren image is an indirect measure of the magnitude of the spatial gradient of density, resulting in a change in the refractive index of the flow. Therefore, different flow structures can be distinguished by the  $I_{\text{rms}}$ . The  $I_{\text{rms}}$  is calculated using the pixel intensity matrix of the  $k$ th schlieren image  $I_k$  and the  $I_{\text{mean}}$  using the following equation, where  $N$  represents the number of images:

$$I_{\text{rms}} = \sqrt{\sum_{k=1}^N (I_k - I_{\text{mean}})^2 / N} \quad (1)$$

It should be noted that the residual quantity  $\varepsilon$ , which is defined as the maximum absolute difference between  $I(i,j)_{\text{mean}}^N$  or  $I(i,j)_{\text{rms}}^N$  derived from several schlieren snapshots, should converge to a slightly smaller magnitude than 0.1, which can be regarded as the uncertainty of the quantity. To ensure the convergence of the quantity, we acquired 20,000 images using the high-speed schlieren system for analysis.

Tektronix P6015A was used for voltage measurements, and Tektronix TCP312 was used for current measurements, respectively. The waveforms were collected by a Tektronix DPO4104 with a 5GS/s sampling rate.

The particle laser scattering (PLS) technique is used for flow visualization by using water molecule as tracing particles that are the same magnitude in size of the nanoparticles used by Zhao et al. (2009). This technique has been used for visualizing a swept shock wave/boundary-layer interaction and shows well observation (Qinghu et al. 2020). The effectiveness of water vapor has been validated by Stever et al.

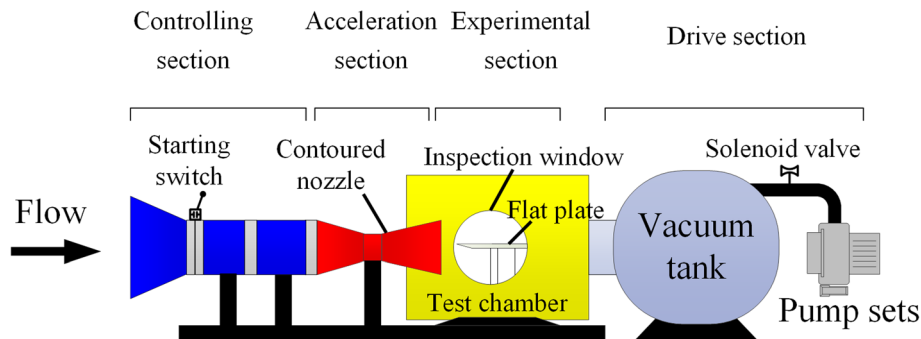
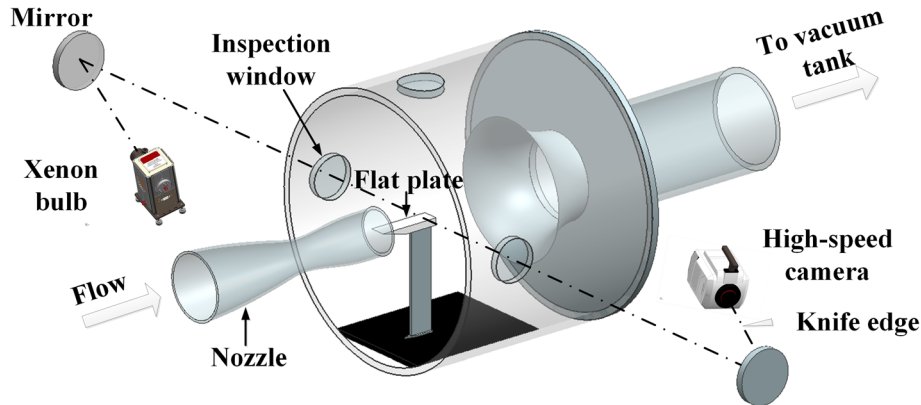


Fig. 1 Schematic diagram of the supersonic wind tunnel structure

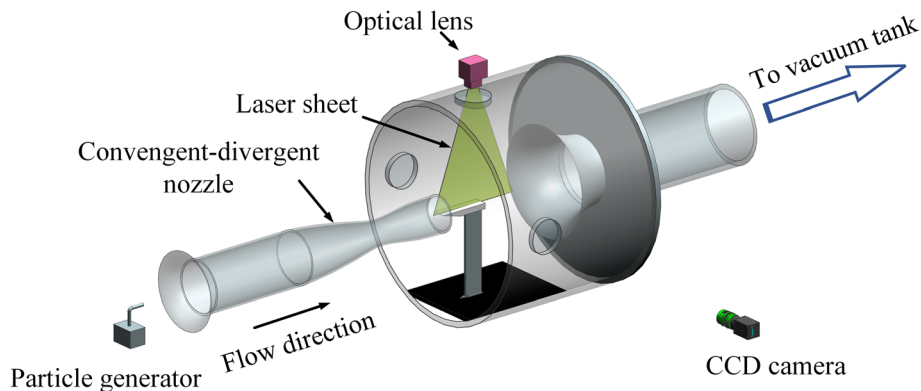
**Table 1** Flow parameters

Parameter	Value
Ma	2
$U_\infty$ (m/s)	513
$P_0$ (kPa)	95.6
$T_0$ (K)	296
$P_s$ (kPa)	12.24
$T_s$ (K)	164

**Fig. 2** The schlieren system

(2016). The illumination system is a V-shot 450 dual-head ND: YAG pulsed laser with a maximum frequency of 10 Hz, which produces a laser sheet light with a thickness of 1 mm and a maximum single pulse energy of 450 mJ. The laser pulses are separated by 1  $\mu$ s. The images are recorded using a LaVision CCD camera (Imager pro x200M) in dual exposure mode. The water vapor is generated by an ultrasonic humidifier with an exit in front of the wind tunnel. In order to increase the water vapor concentration, the outside atmospheric is humidified in advance. The sketch of the PLS system is illustrated in Fig. 3. As injected water vapor subjected to a cold condensation due to a sudden temperature drop after accelerated by the divergent nozzle, nanometer-sized water particles are formed in the test section which can be illuminated by the intense laser sheet. Thus, the microscopic morphology of the thermal gas bubble (TGB) is revealed as it has lower density and higher temperature, causing the condensed water molecules around the TGB to sublimate and exhibit darker compared with the freestream region.

Two types of SWBLI were tested in the experiment (as shown in Fig. 4), namely, an incident shock wave/boundary-layer interaction (ISWBLI) and a ramp-induced shock wave/boundary-layer interaction (RSWBLI). A flat plate with a size of 250  $\times$  110 (mm) was used to develop the boundary layer. The incident shock is generated by a wedge (10-degree) hanging over the flat plate, and the ramp shock is

**Fig. 3** The PLS system

generated by a 30-degree ramp assembled on the flat plate, respectively. The actuators array that consists of four actuators is placed upstream the interaction region in spanwise direction with a space of 10 mm. Each actuator contains two copper electrode sticks (3 mm diameter) flush-mounted into the flat plate with a gap of 7 mm edge-to-edge.

### 3 Results and discussion

#### 3.1 Discharge properties

The details of the power system and the circuit can be referred to reference (Gan and Wang 2022). It is concluded that high-frequency enables a stable control effect in the experiment. Thus, in rest part of the paper, the actuation frequency of all actuator arrays was empirically set 10 kHz to investigate the separation control effect on the two interaction types. Figure 5 depicts the current–voltage waveform in one pulse. The discharge voltage reaches 13 kV in a short time less than 0.1  $\mu$ s, and then, it drops rapidly to less than 0 in about 0.3  $\mu$ s. The current waveform is fairly similar with the voltage. It takes 0.1 s to reach a peak of roughly 82 A after the air breakdown and then, gradually drops to zero.

#### 3.2 PLS results

The PLS results (Fig. 6) of a ramp-induced SWBLI with 10 kHz actuation are first examined while the ISWBLI results are not revealed here because the laser sheet has no access to the interaction region due to the wedge hanging over the plate. In order to avoid the strong influence of discharging on the measurement devices, a delay time of 15  $\mu$ s was set for the CCD camera. Note that the first snapshot is denoted as the temporal origin. A dark region can be found at  $x = -35$  mm upstream the corner which suggests the initial formation of thermal gas bubble array after the discharge. A weak blast wave also can be detected in the first snapshot. The thermal gas bubbles followed the flow downstream to interact with the SWBLI region. The head of TGBs reached  $x = -15$  mm after 30  $\mu$ s later, as shown in Fig. 6b, after which a trailing of small vortices is also observed close to the wall. These trailing vortices were confirmed to be separated from the original TGBs (Gan and Wang 2021). In the following snapshot, these trailing vortices have already interacted with the SWBLI which result in substantial turbulent eddies and a thickened interaction region. It

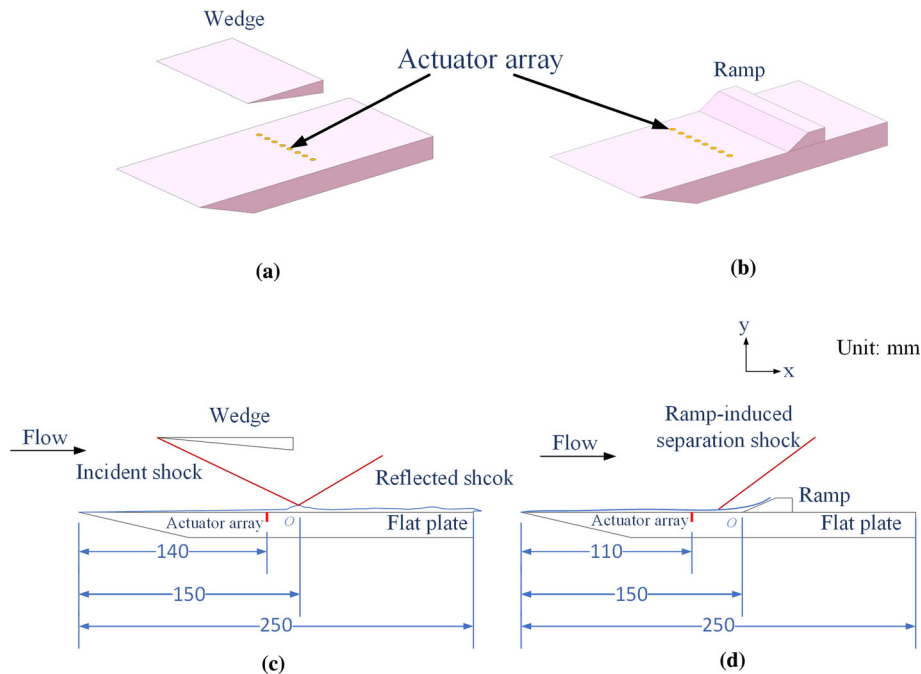


**Fig.4** The experimental model

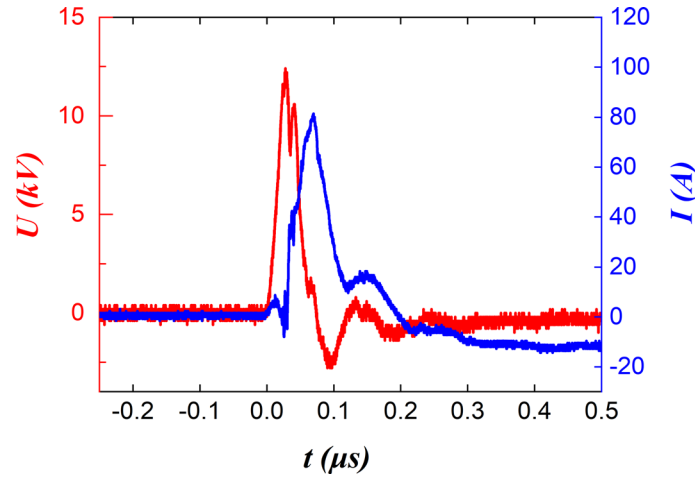


**Fig. 5** Voltage and current waveform for a single pulse at 10 kHz

is then detected that the separation shock foot is removed by the TGBs and the trailing vortices, indicating the shock intensity reducing effect. The TGBs and their trailing vortices are completely turbulized as they reached the ramp surface at  $t = 50 \mu\text{s}$  which is indicated by the thickened shaded area around the ramp corner. However, the TGB head is failed to resolve at this moment due to the highly turbulent near-wall region on the ramp surface. In the next snapshot at  $t = 60 \mu\text{s}$ , the merged TGBs move over the ramp surface and finally, exit the field of vision, but the trailing vortices continue to affect the corner region where the separation bubble located. After that, a decrease in dark region can be observed at  $t = 70 \mu\text{s}$ , which indicated an inhibition of separation induced by RSWBLI. However, further solid evidence of separation control through direct PIV measurements is needed. In addition, the separation shock is not completely recovered to the unaffected state, which indicated that a stable control effect can be achieved by activating another perturbation as fast as possible.

### 3.3 Schlieren image results

The controlling process of the RSWBLI at the  $30^\circ$  compression ramp is represented through four instantaneous schlieren snapshot in Fig. 7. In order to capture spatial motion of the flow induced by the discharge, the time interval was set to be  $20 \mu\text{s}$ . It should be noted that the trigger of high-speed camera recording is set as the start of the wind tunnel, so the schlieren images do not overlap with the PLS results. For the convenience of discussion, the first snapshot is labelled here as the temporal origin. At  $t = 0 \mu\text{s}$ , the separation shock wave is more obvious in these schlieren images than it is in the PLS data, appearing as a dark line upstream of the ramp corner. The TGBs are also visualized at  $x = 35 \text{ mm}$  with an umbrella-type blast wave. As the TGBs approach the interaction region at  $t = 20 \mu\text{s}$ , they move upward after its interaction with the separation shock. However, these trailing vortices observed in the PLS results are unapparent at this moment. The turbulent region on the ramp appears to be enhanced significantly by the TGBs at  $t = 40 \mu\text{s}$ . In addition, a small undulation of the separation shock foot can be observed while it interacts with the flickering waves of the TGBs which manifests the exiting of trailing vortices. In the following snapshot  $t = 60 \mu\text{s}$ , the merged TGBs transformed to a turbulent structure moving across the ramp surface. Figure 8 represents a mean intensity of 3000 frames for baseline and 10 kHz forcing. It is observed that the separation shock foot is indistinct, which appears to be blending in with the background. In addition, it can be identified clearly that the angle of separation shock decreases by 3 degrees according to the dashed line in Fig. 8. As the intensity of the separation shock is positively correlated with its angle, the boundary layer is subjected to a less intense adverse pressure gradient that imposed by the shock which, in turn, may causes the interaction strength decrease and separation region to shrink. The ability of SAPAs to reduce shock wave intensity is proved to be feasible, but the separation region shrink needs further verification by some other quantitative measurements.

The  $I_{\text{rms}}$  for RSWBLI control is shown in Fig. 9. It has a range of 0–25 counts. These contours were selected to determine the  $I_{\text{rms}}$  distribution around the corner which is an indirect reflect of separation control effect. The results of 10 kHz forcing show substantial differences between the control case and the baseline.

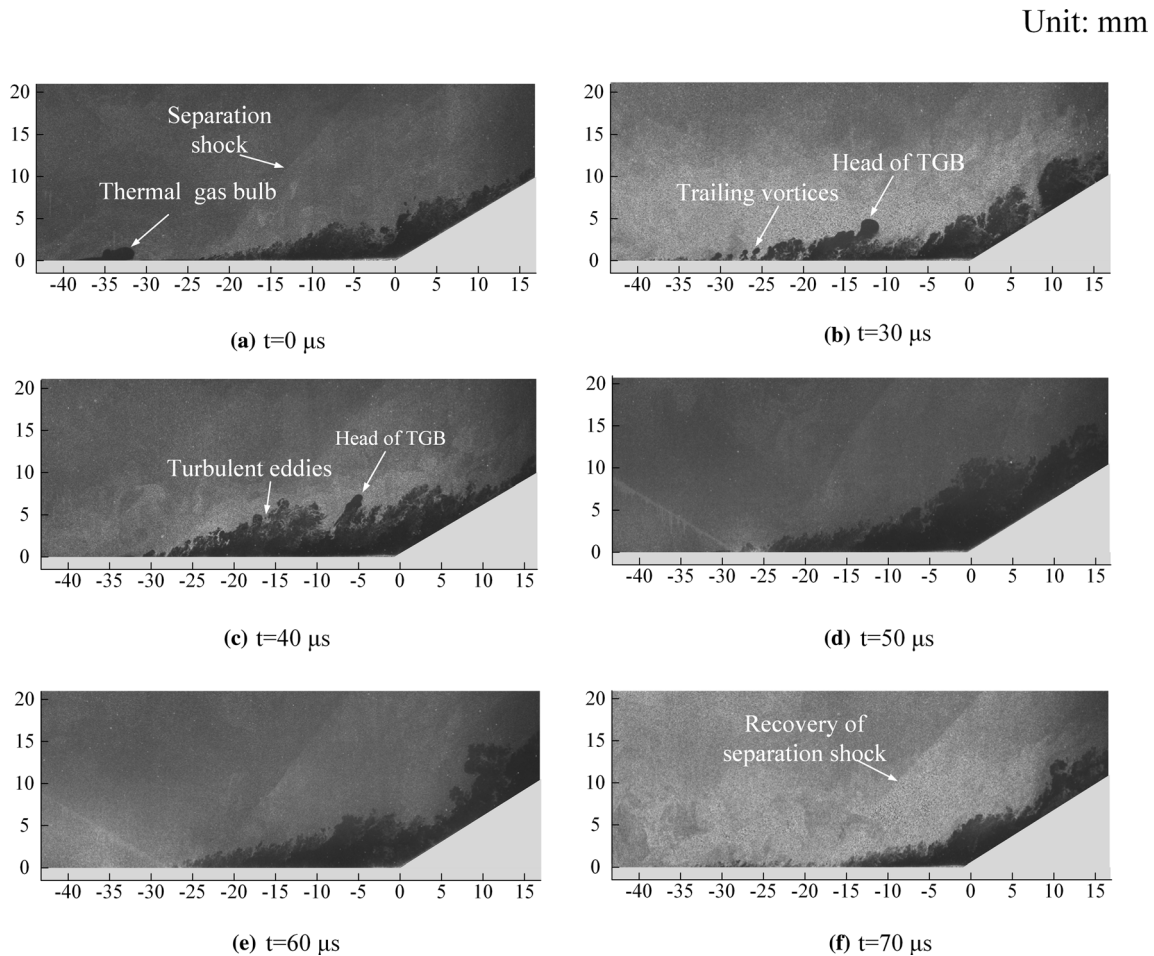


**Fig. 6** The temporal evolution of the flow controlled by SAPAs

A lower  $I_{\text{rms}}$  can be distinct around the corner in both cases indicating a small fluctuation of velocity, and this region is speculated as the area of separation bubble, which is more stable than the surrounding places with strong fluctuation of velocity. A blue trip with higher  $I_{\text{rms}}$  is produced over the separation bubble which refers to the turbulent shear layer and flow over the ramp. Thus, an encouraging result is revealed by the  $I_{\text{rms}}$ , and the separation bubble is inhibited in the actuation case. In the controlling case, the contraction of the separation bubble is accompanied with the growth of the turbulent region which manifest the increase in small vortices in PLS results. The schlieren results confirm the excellent performance for flow topology visualization.

The instantaneous schlieren snapshot of IWBLI controlled by SAPAs is shown in Fig. 10. The TGBs are lifted up while passing through the interaction region because of retarding effect induced by the separation region. The turbulent flow after the interaction region is enhanced by the actuation due to the arise of trailing vortices. The reflected shock shows a smaller undulation while the incident shock seems not to be affected by the TGBs. Concerning the boundary layer behavior, there are no basic differences among the interaction with an incident shock, a ramp shock and a normal shock. Thus, the underlying vortex controlling mechanism is universal.

The  $I_{\text{rms}}$  of baseline and 10 kHz forcing for ISWBLI control is shown in Fig. 11. For the baseline, the boundary layer upstream the interaction region looks like a thin and uniform strip which can be deduced as a laminar state. A lower magnitude of  $I_{\text{rms}}$  is also present at the bottom of the interaction region which can be speculated as a separation bubble. The thickness of the boundary layer is greater downstream of the interaction region as the turbulence increases. The results of 10 kHz forcing also show substantial differences from the baseline. The formation of thermal gas bubbles causes trailing vortices associated with a strong shear effect downstream of the actuators. These streamwise vortices interact with the initial boundary

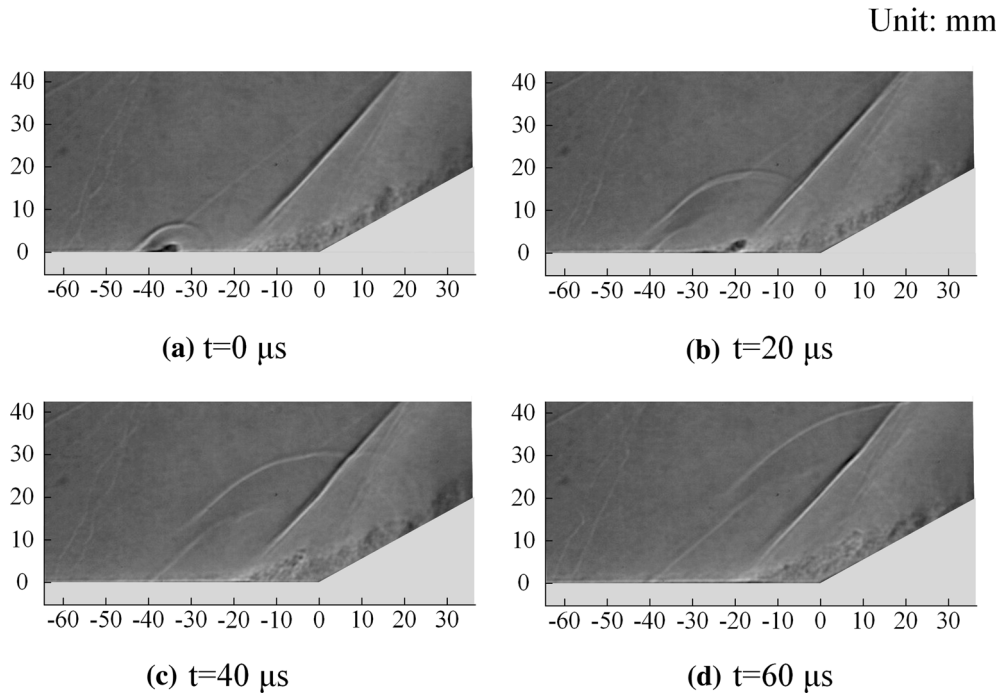


**Fig. 7** Shadowgraph images of the TGBs and the RSWBLI in a  $Ma = 2$  flow

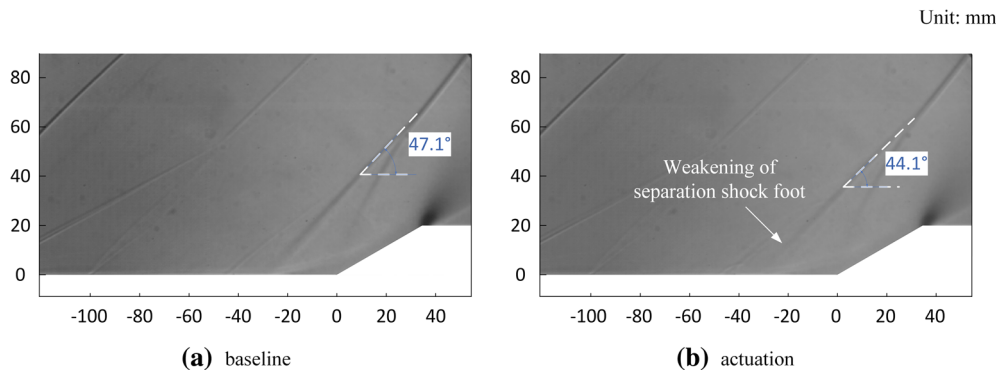


**Fig. 8** The mean schlieren intensity field ( $I_{\text{mean}}$ )

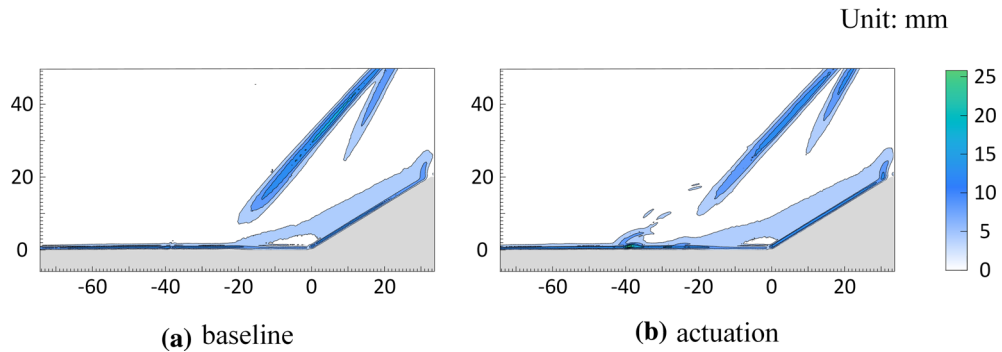


**Fig. 9** The RMS of the schlieren intensity field ( $I_{\text{rms}}$ ) of RSWBLI for the baseline (left) and 10 kHz forcing (right)



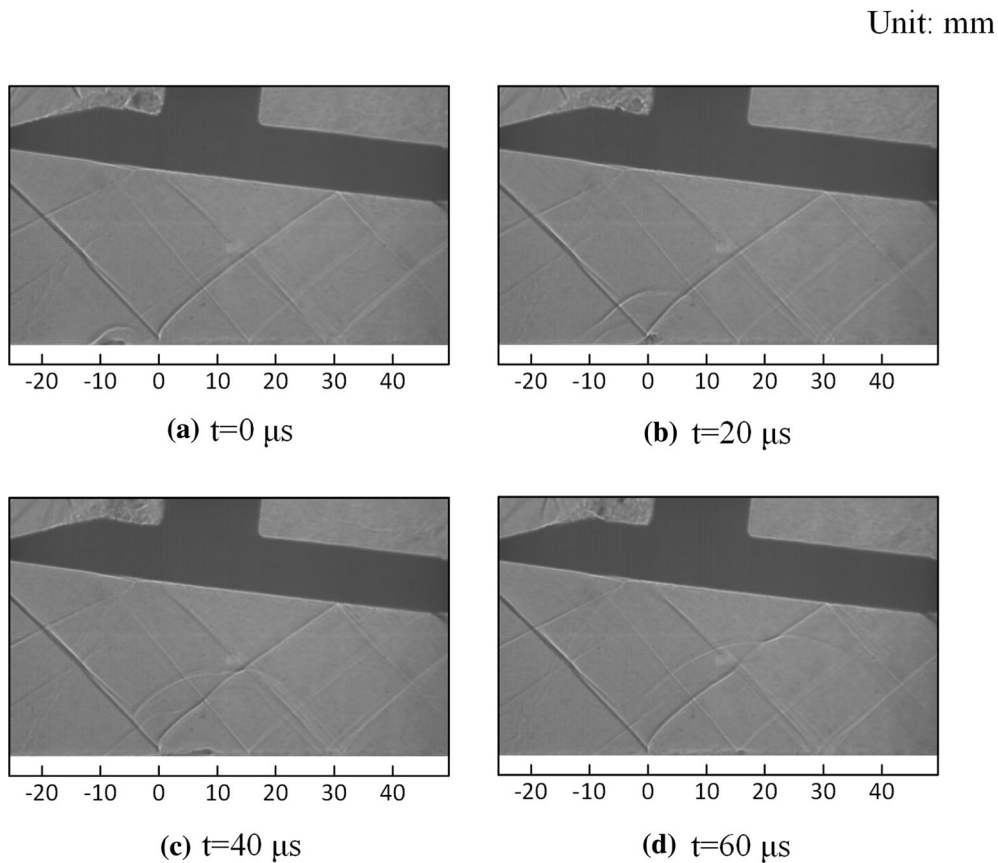


**Fig. 10** Shadowgraph images of the TGBs and the ISWBLI in a  $Ma = 2$  flow

layer first, suggesting significant vortical activity in the boundary layer, whose thickness increases immediately according to the  $I_{rms}$  intensity. Amplification and breakdown of these disturbances eventually lead to a more turbulent boundary layer which carries more momentum. Hence, there is greater resistance to the retardation imparted by the incident shock and separation. Consequently, the separation bubble of ISWBLI labeled as a low magnitude of  $I_{rms}$  in the baseline has been removed by applying SAPAs with high actuation frequency.

### 3.4 Manipulation of low-frequency shock motion

The instability of supersonic inlet is mainly produced by the shock–shock interaction or SWBLI at lip of the inlet. And it has strong correlation with the low-frequency band of SWBLI unsteadiness. It also accelerated the fatigue of aircraft structure as fluctuating load is increased by the low-frequency unsteadiness.

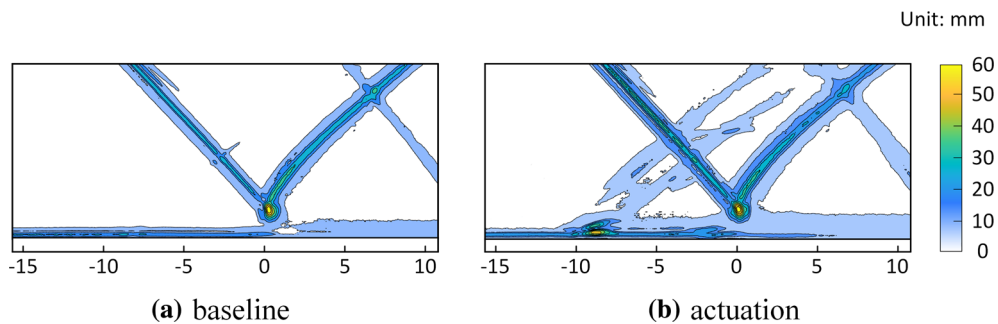


**Fig. 11** The RMS of the schlieren intensity field ( $I_{rms}$ ) of ISWBLI for the baseline (left) and 10 kHz forcing (right)

Developing techniques for control of low-frequency, large-scale shock motions has attracted the most interest over the past two decades. Herein, we examined the shock motion variation of RSWBLI while applying SAPAs by using schlieren processing method. The schlieren processing method proposed by Schmidt and Shepherd (2015) is used to extract the shock position in this paper. The frequency characteristics of separation shock motion were obtained by extracting the point with the maximum gray difference in the schlieren sequence. Figure 12b shows the variation of image intensity along the white dashed line in Fig. 12a. A distinct abrupt drop-off followed by a peak can be detected. This characteristic is being used to locate the shock for each image. To investigate the motion of the shock, we extracted the maximum intensity from a time series images at a certain height corresponding to the white dashed line. And those data were reconstructed to time–space maps as shown in Fig. 12c. The vertical axis is  $x/20$ , and the horizontal axis is the time from 0.20 s to 0.24 among the test. The red line and blue line are corresponding to the shock motion without plasma actuation and with an actuation frequency of 10 kHz, respectively. The characteristic of separation shock can be reflected distinctly in intensity variation. The location information of the behaviors is well captured.

The separation shock does not oscillate in a periodical way in both cases suggesting a strong coupling with some other unsteady aspects of SWBLI. In 10 kHz forcing, the separation shock was forced to move upstream according to forward-moving mean shock location. Both large-scale motion in Fig. 12d and small-scale motion in Fig. 12e are detected which manifest the existing of multi-scale vortices in the interaction region.

It is obviously from the above discussion that the induced streamwise vortices cause the separation shock to respond to the forcing frequency. To quantify this effect further, we are using Fourier analysis to process the data of shock trajectory. The shock motion spectrum and dominant frequency can be extracted via this method. In this paper, we acquired the images of 0.4 s for actuation condition which means it has 20,000 samples of shock position for each measurement series. A fast Fourier transform (FFT) was applied to determine the frequency spectra of the shock motion. The data length was 0.4 s, so the frequency resolution was 2.5 Hz. The combination of the high-speed camera and visualization-schlieren system made it possible for us to investigate the low-frequency separation shock behaviors in compression ramp flow quantitatively.

To reveal more frequency information for separation shock with and without plasma actuation, we added the power spectrum density (PSD) functions of baseline for comparison, as shown in Fig. 13a. The dominant frequency and its spectrum were extracted from the shock motion by Fourier analysis. To highlight the characteristics of shock frequency, the power spectra for shock motion are presented in the terms of  $f \times P(f)$

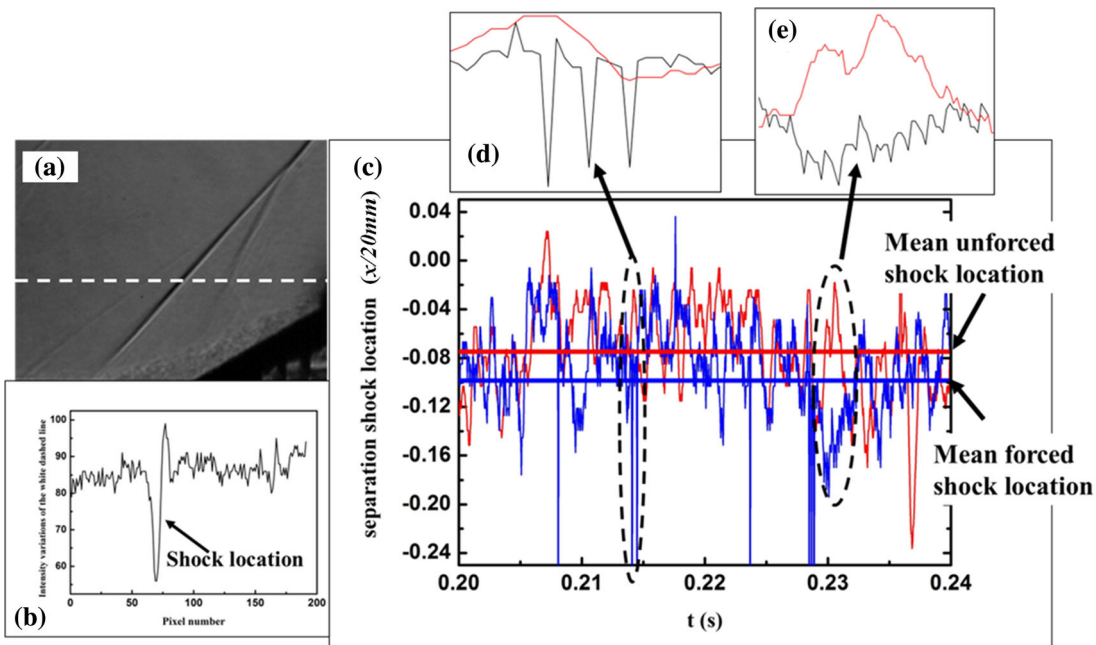


**Fig. 12** a Method for shock motion location extraction, b shock motion trajectory with time, c shock location histories: with actuation (blue line), and baseline (red line)

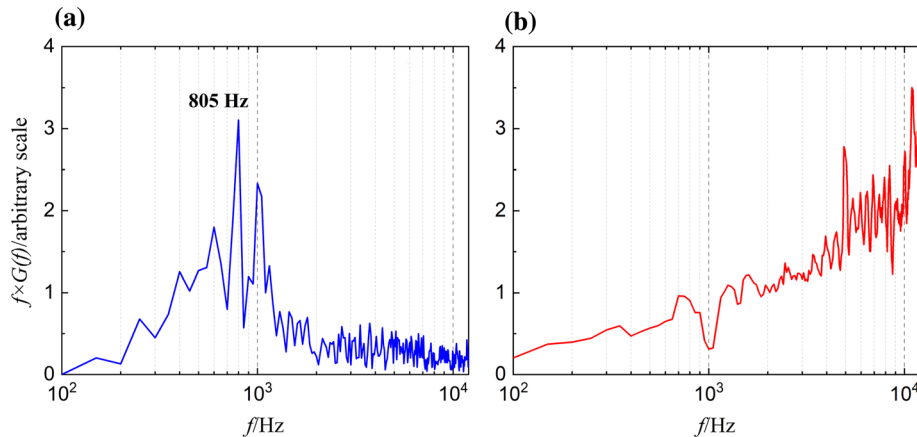


**Fig. 13** Comparison between the spectra of separation shock motion with and without forcing: **a** baseline; **b** actuation

versus  $\log(f)$  in which  $P(f)$  is the power spectral density and  $f$  is a temporal frequency. Figure 13 (a) and (b) shows the distribution of PSD function of separation shock with and without plasma actuation, respectively. In each plot, spectra of the shock motion without forcing are clearly seen. The dominance frequency of shock foot motion is 805 Hz.

From Fig. 13, when plasma actuation is activated, the spectra have been dramatically changed compared with the basic condition without control. An apparent frequency shifting for separation shock is observed in the graphic. In basic SWBLI, the dominance oscillation frequency was observed to be 805 kHz and not any higher frequency motions were detected. The dominance frequency value increased to a magnitude of 10 kHz with actuation. In addition, more frequency peaks were detected and the power spectrum of separation shock oscillation occupies a wide frequency band which indicates a part of low-frequency energy shift to high-frequency band.

#### 4 Conclusion

In this paper, a surface arc plasma actuator array is used for controlling the shock wave/boundary-layer interaction. Two models including a ramp corner and a wedge over a flat plate are designed to provide a featured flow field, containing a ramp-induced shock wave/boundary-layer interaction and an incident shock boundary layer interaction. The schlieren diagnostics and PLS technique are used to reveal the flow characteristic with and without actuation. The main conclusions are summarized as follows:

- (1) Based on the schlieren results and PLS results, substantially trailing vortices are produced after the main gas bulb generated by the SAPAs which increases the local vortical activity and the state of the boundary layer.
- (2) The  $I_{\text{rms}}$  results show that the separation region of RSWBLI with SAPAs is comparatively smaller than the baseline without control. For ISWBLI, the separation region is also substantially decreased by the actuation according to the  $I_{\text{rms}}$  results, the contraction of the separation bubble that is ISWBLI is accompanied with the growth of the turbulent region. But it should be noted that this is not a universal conclusion for all type of shock wave/boundary-layer interaction because they have different flow topology and strength. Thus, specific analysis should be made according the practical interaction type.
- (3) The separation shock oscillates in low-frequency mode in the baseline of RSWBLI. When plasma actuation is activated, the spectra have been dramatically changed compared with the basic condition without control. An apparent frequency shifting for separation shock is also observed in RSWBLI.

**Acknowledgements** The authors gratefully acknowledge the National Natural Science Foundation of China for financial support to this work under Grant NSFC No. 11902360 and CPSF (China Postdoctoral Science Foundation) No. 2021M702676.

**Open Access** This article is licensed under a Creative Commons Attribution 4.0 International License, which permits use, sharing, adaptation, distribution and reproduction in any medium or format, as long as you give appropriate credit to the original author(s) and the source, provide a link to the Creative Commons licence, and indicate if changes were made. The

images or other third party material in this article are included in the article's Creative Commons licence, unless indicated otherwise in a credit line to the material. If material is not included in the article's Creative Commons licence and your intended use is not permitted by statutory regulation or exceeds the permitted use, you will need to obtain permission directly from the copyright holder. To view a copy of this licence, visit <http://creativecommons.org/licenses/by/4.0/>.

## References

- Clemens NT, Narayanaswamy V (2014) Low-frequency unsteadiness of shock wave/turbulent boundary layer interactions. *Annu Rev Fluid Mech* 46:469–492
- Gan T, Wang Q (2021) Mechanisms of SWBLI control by using a surface arc plasma actuator array. *Exp Therm Fluid Sci* 128(1):110428
- Gan T, Wang Q (2022) Manipulation of ramp-induced shock using an array of surface arc plasma actuators. *Int J Heat Fluid Flow* 93:108894
- Gan T, Jin D, Wu Y et al (2018a) Influence of ambient pressure on the performance of an arc discharge plasma actuator. *Contrib Plasma Phys* 58(4):260–268
- Gan T, Wu Y, Sun ZZ et al (2018b) Shock wave boundary layer interaction controlled by surface arc plasma actuators. *Phys Fluids* 30:055107
- Hadjadj A, Dussauge JP (2009) Shock wave boundary layer interaction. *Shock Waves* 19(6):449–452
- Huang J, Yao WX (2020) Active flow control by a novel combinational active thermal protection for hypersonic vehicles. *Acta Astronaut* 170:320–330
- Huang W, Wu H, Yang YG et al (2020) Recent advances in the Shock wave/boundary layer interaction and its control in internal and external flows. *Acta Astronaut* 174:103–122
- Im S, Do H, Cappelli MA (2010) Dielectric barrier discharge control of a turbulent boundary layer in a supersonic flow. *Appl Phys Lett* 97(4):605
- Kim JH, Nishihara M, Adamovich IV et al (2010) Development of localized arc filament RF plasma actuators for high-speed and high Reynolds number flow control. *Exp Fluids* 49(2):497–511
- Liao Y, Mursenkova IV, Ivanov IE et al (2020) Shock waves generated by a pulsed surface sliding discharge in a supersonic airflow past a wedge. *Phys Fluids* 32(10):106108
- Luo YH, Liang H, Li J et al (2022) Experimental investigation of incident Shock wave/boundary layer interaction controlled by pulsed spark discharge array. *Exp Therm Fluid Sci* 132:110515
- Ma X, Fan J, Yunkai Wu et al (2022) Study on the mechanism of Shock wave/boundary layer interaction control using high-frequency pulsed arc discharge plasma. *Phys Fluids* 34:086102
- Maeno K, Ogawa K, Kawanobe Y (2000) Color schlieren photographs of interaction between oblique Shock wave and boundary layer on flat plate with bleeding effect. *J vis* 2:211
- Narayanaswamy V, Raja LL, Clemens NT (2012) Control of unsteadiness of a Shock wave/turbulent boundary layer interaction by using a pulsed-plasma-jet actuator. *Phys Fluids* 24:076101
- Qinghu Z, Zhiwei Z, Jingzhou L et al (2020) Visualization of hypersonic incident Shock wave boundary layer interaction. *J Vis* 23:207–214
- Schmidt BE, Shepherd JE (2015) Oscillations in cylinder wakes at Mach4, *Journal of Fluid Mechanics* 785
- Stever HG (2016) Condensation phenomena in high speed flows. *Fundamentals of gas dynamics, vol 3 [J]*. Princeton University Press Princeton NJ, 1958:526–573
- Tang MX, Wu Y, Wang HY et al (2018) Characterization of transverse plasma jet and its effects on ramp induced separation. *Exp Therm Fluid Sci* 99:584–594
- Tang MX, Wu Y, Zong HH (2022a) Experimental investigation of supersonic boundary-layer tripping with a spanwise pulsed spark discharge array. *J Fluid Mech* 931(16):7
- Tang M, Wu Y, Wang H (2022b) Experimental investigation on hypersonic shock-shock interaction control using plasma actuator array. *Acta Astronaut* 198:577–586
- Wang H, Li J, Jin D et al (2018) High-frequency counter-flow plasma synthetic jet actuator and its application in suppression of supersonic flow separation. *Acta Astronaut* 142:45–56
- Wang H, Weibo Hu, Xie F et al (2022) Control effects of a high-frequency pulsed discharge on a hypersonic separated flow. *Phys Fluids* 34:066102
- Webb N, Clifford C, Samimy M et al (2013) Control of oblique Shock wave/boundary layer interaction using plasma actuators. *Exp Fluids* 54:1545
- Wu Y, Li Y (2015) Progress and outlook of plasma flow control. *Acta Aeronautica et Astronautica Sinica* 36(2):381–405
- Xie W, Luo ZB, Zhou Y et al (2021) Experimental study on shock wave control in high enthalpy hypersonic flow by using sparkjet actuator. *Acta Astronaut* 188:416–425
- Yan H, Gaitonde D (2010) Effect of thermally induced perturbation in supersonic boundary layers. *Phys Fluids* 22(6):064101
- Yang H, Zong H, Liang H, Yun Wu, Zhang C, Kong Y, Li Y (2022) Swept shock wave/boundary-layer interaction control based on surface arc plasma. *Phys Fluids* 34:087119
- Zhang Y, Chen L, Tan HJ et al (2021) Visualization of curved swept shock wave/turbulent boundary layer interaction in supersonic flow. *J Vis* 24:1–7
- Zhao YX, Yi SH, Tian LF (2009) Supersonic flow imaging via nanoparticles. *Sci China Ser E Technol Sci* 52(12):3640–3648